Enhancing the Thermoelectric and Mechanical Properties of P-type PbS through Band Convergence and Microstructure Regulation

Mengyao Li[1], Dongyang Wang[1], Xu Han[2], Dawei Yang[3], Xueke Zhao[1], Benteng Wu[1], Mochen Jia*[1], Hongzhang Song[1], Yu Liu[4], Jordi Arbiol,[2,6] Andreu Cabot*[5,6]*

[1] School of Physics and Laboratory of Zhongyuan Light, Zhengzhou University, Zhengzhou 450001, China.

[2] Catalan Institute of Nanoscience and Nanotechnology (ICN2), CSIC and BIST, Campus UAB, Bellaterra, 08193 Barcelona, Catalonia, Spain.

[3] Henan Province Key Laboratory of Photovoltaic Materials, School of Future Technology, Henan University, Kaifeng, 475004, P. R. China.

[4] Anhui Province Key Laboratory of Advanced Catalytic Materials and Reaction Engineering, School of Chemistry and Chemical Engineering, Hefei University of Technology, 230009, Hefei, China.

[5] Catalonia Institute for Energy Research-IREC, Sant Adrià de Besòs, 08930 Barcelona, Spain.

[6] ICREA, Pg. Lluís Companys 23, 08010 Barcelona, Catalonia, Spain.

ABSTRACT: Lead sulfide (PbS) shows notable thermoelectric properties as well as a relatively stable lattice structure. Nonetheless, the production cost of PbS materials remains relatively high, and its mechanical hardness is low, thus constraining its widespread application and commercial viability. In this study, we demonstrate a straightforward, cost-effective synthesis method at ambient temperature to produce PbS nanocrystals. By introducing controlled amounts of silver doping, we achieve p-type conductivity and fine-tune both the energy band structure and lattice configuration. Density functional theory (DFT) calculations show the introduction of silver shifts the Fermi surface into the valence band, facilitating band convergence and thereby enhancing the power factor. Besides, excess silver is present in the secondary phase of silver sulfide, which effectively diminishes the interface barrier and thereby enhances the Seebeck coefficient. The defects caused by doping, along with the dislocations and multiple interfaces introduced by secondary phases, effectively scatter phonons, reducing thermal conductivity to an ultra-low value of 0.49 W $m^{-1}K^{-1}$ at 690 K. Moreover, the alterations in crystal structure and chemical composition within the composite contribute to improving its mechanical properties. Overall, optimized materials reach dimensionless thermoelectric figures of merit (*ZT*) approximately ten times higher than pristine PbS at 690 K, alongside boasting a remarkable average hardness of 1.08 GPa at room temperature.

KEYWORDS: lead sulfide, energy band regulation, structural engineering, lattice thermal conductivity, mechanical hardness.

Thermoelectric materials enable the direct energy conversion between heat and electrical by exploiting the motion of charge carriers within solids. They hold significant promise for applications in green energy, space exploration, and solid-state refrigeration technologies. The efficiency of a thermoelectric device hinges on the resulting temperature gradient and three closely linked physical parameters: conductivity (σ), Seebeck coefficient (S), and thermal conductivity (κ). These parameters combine into a dimensionless figure of merit for thermoelectric performance, denoted as ZT, and calculated by the formula: $ZT=\sigma S^2T/\kappa$. Consequently, achieving high-performance thermoelectric materials necessitates traits such as elevated conductivity, significant Seebeck coefficient, and minimal thermal conductivity.

Optimizing the electrical performance and Seebeck coefficient requires balancing the relationship between carrier concentration (n, p), carrier mobility (μ) and effective mass (m^*). To maximize the power factor (PF) of intrinsic semiconductor materials, doping becomes imperative for optimizing carrier concentration and electronic band structure[1–7]. For instance, p-type SnSe undergoes doping to modulate its energy band structure[8–10], resulting in an increased n of approximately $\sim 10^{19}$ cm^{-3}, thereby significantly enhancing its σ. Conversely, semiconductors with inherently high carrier concentration, like SnTe and $Cu_{2-x}S$, require alterations in the lattice structure through doping[11] or the incorporation of a second phase[12] to mitigate n. Through mechanisms such as state density resonance[13], energy band degeneracy[14], and energy band convergence[15], thermoelectric materials with low m^* can achieve significant enhancements in both m^* and S.

Thermal conductivity is influenced by carrier thermal conductivity (κ_{ele}), lattice thermal conductivity (κ_L), and bipolar diffusion thermal conductivity (κ_b). κ_L can be diminished by constraining phonon modes across all wavelength segments through multi-scale layered architecture designs[16–20]. Techniques including point defect scattering, dislocation scattering, grain boundary scattering, resonance scattering, and electroacoustic scattering are employed for this purpose.

Overall, optimizing the composition, tuning defects, refining lattice structure, and engineering energy bands are effective strategies for enhancing the *ZT* value of semiconductor thermoelectric materials. These approaches facilitate coordinated control over n, μ, and κ_L, thereby improving overall performance.

PbX (X=Te, Se, S) is a typical medium-temperature thermoelectric material and has been widely studied due to its superior thermoelectric properties. Among Pb chalcogenides, PbS is based on particularly abundant natural resources that makes it potentially cost-effective in numerous commercial applications[21]. However, PbS has relatively high κ_L and modest *PF*, which can be improved through doping and interface engineering. Doping can effectively adjust the electronic structure and energy band characteristics[22–27], control the n and S, and thereby improve the *PF*. Besides, interface engineering can effectively scatter multi-scale phonons and reduce κ_L. Additionally, PbS exhibits poor mechanical hardness, which poses challenges to both its preparation and practical applications, particularly in the context of device miniaturization.

Here, we present a straightforward approach for synthesizing PbS nanocrystals, coupled with a novel method to tailor the position of the Fermi level through silver doping, thereby imparting *p*-type semiconductor characteristics. By fine-tuning the silver content, the energy band convergence is promoted, leading to a boost in the m^*, consequently optimizing the *PF*. Additionally, the presence of silver introduces defects and increases the density of grain boundaries, which effectively scatter phonons, thereby reducing κ_L. Moreover, the defects and secondary phases induced by Ag doping generate additional dislocations and blocking points within the material. These features serve to impede atomic movement within the crystal lattice, consequently enhancing the material's hardness.

PbS nanocrystals were prepared by the reaction of $Pb(CH_3COO)_2 \cdot 3H_2O$ and $(NH_4)_2S$ at ambient temperature and conditions within an aqueous solvent (**Figure S1**). Further details regarding the synthesis procedure can be found in the Supplementary Information (SI). The reaction yields nanocrystals with an average size of approximately 17 nm (**Figure S2**). XRD analysis revealed the particles to exhibit a

distinctly crystalline cubic PbS structure, as shown in **Figure S2c**. High-resolution transmission electron microscopy (HRTEM) analysis of the crystal displayed in **Figure S2d** show the PbS lattice fringes to be 0.344 nm, 0.330 nm, and 0.296 nm, at 70.39º and 120.78º. These values correspond to the cubic PbS phase, observed along its [1-10] zone axis.

$Pb_{1-x}Ag_xS$ (x=0, 0.03, 0.05, and 0.10) nanoparticles were produced by the reaction of proper amounts of $Pb(CH_3COO)_2$ and $AgNO_3$ with $(NH_4)_2S$ in water and at ambient temperature, pressure and atmosphere. The XRD pattern of the $Pb_{1-x}Ag_xS$ nanopowders revealed the presence of the cubic PbS phase, with no discernible peaks indicating the presence of additional Ag or Ag_xS phases, which could be attributed to the low content of silver. The XRD diffraction peaks of the Ag-doped samples shift towards higher angles, indicating that Ag^+, with a smaller ionic radius, partially replace Pb^{2+}, within the PbS lattice, which results in a reduction in the lattice parameters. However, with increasing silver content, the diffraction peak shift reaches a plateau, suggesting that the solubility of silver has reached saturation (**Figure 1a and 1b**). Within the experimental error of the technique, SEM-EDX analysis revealed a strong correlation between the observed amount of silver within the material and the nominal amount introduced (**Figure S3** and **Table S1**). Thus, at high Ag loadings, the excess silver must exist within the material in the form of secondary phase.

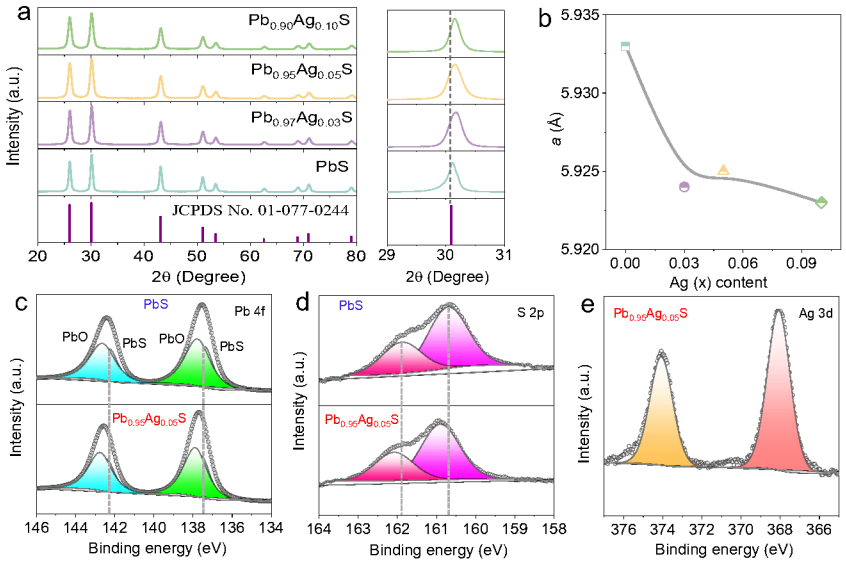

Figure 1. a) XRD patterns of the $Pb_{1-x}Ag_xS$ nanoparticles, and magnification of the (200) XRD peak. b) Experimental lattice parameters calculated from XRD patterns. c-e) High resolution Pb 4f (c), S 2p (d) and Ag 3d (e) XPS spectra of $Pb_{0.95}Ag_{0.05}S$.

The high-resolution XPS spectra of PbS and $Pb_{0.95}Ag_{0.05}S$ nanoparticles are shown in **Figure 1c-e**. The bands observed at 142.2 and 137.4 eV correspond to the Pb $4f_{5/2}$ and Pb $4f_{7/2}$ core levels, of Pb^{2+} cations within the PbS chemical environment[24]. The bands at 142.6 and 137.8 eV are attributed to the Pb 4f core levels of Pb^{2+} within a PbO chemical environment[24]. The PbO presence indicates partial surface oxidation of the material upon exposure to the ambient atmosphere. In the $Pb_{0.95}Ag_{0.05}S$ sample, the peak positions of Pb^{2+} shift to 142.4 and 137.6 eV, respectively. The S 2p XPS spectrum of PbS exhibits two peaks at 161.8 and 160.7 eV, corresponding to the S $2p_{1/2}$ and S $2p_{3/2}$ core levels of S^{2-} within the PbS structure[28]. For the $Pb_{0.95}Ag_{0.05}S$ sample, the peak of S^{2-} positions are also blue-shifted in the same magnitude as the Pb ions, up to 162.0 and 160.9 eV, respectively. The XPS spectra blueshifts obtained with the Ag introduction are associated with the presence of Ag ions with a slightly higher electronegativity than Pb within the lattice and to the related lattice contraction[29–31]. The Ag 3d XPS spectrum of $Pb_{0.95}Ag_{0.05}S$ exhibited two peaks at 374.1 and 368.0 eV, representing the Ag $3d_{3/2}$ and Ag $3d_{5/2}$ core levels of Ag^+ within Ag_2S[32].

Figure 2 shows the representative HRTEM micrographs and the electron energy loss spectroscopy (EELS) elemental composition maps of the $Pb_{0.95}Ag_{0.05}S$ nanoparticles. We observe the presence of Ag to result in a significant particle size reduction, with the average particles size of the $Pb_{0.95}Ag_{0.05}S$ nanoparticles around 12 nm. EELS compositional maps reveal that Pb and S are uniformly distributed within the nanoparticles, but the distribution of Ag appears to be less uniform. **Figure 2b** shows an HRTEM micrograph of a PbS particle within the $Pb_{0.95}Ag_{0.05}S$ sample. For this particle, the PbS lattice fringe distances were measured at 0.289 nm, 0.210 nm and 0.304 nm, at 44.58º and 87.91º which could be interpreted as the cubic PbS phase, visualized along its [100] zone axis. **Figure 2c** displays an HRTEM micrograph taken

from the $Pb_{0.95}Ag_{0.05}S$ sample, revealing the presence of the Ag_2S monoclinic phase (space group = P21/C). Examination of the Ag_2S lattice fringes yielded measurements of 0.337 nm, 0.340 nm, and 0.348 nm, at angles of 56.48º and 117.18º. These parameters are consistent with the monoclinic Ag_2S phase with lattice parameters a=4.2310 Å, b=6.9300 Å, and c=9.5260 Å visualized along its [021] zone axis.

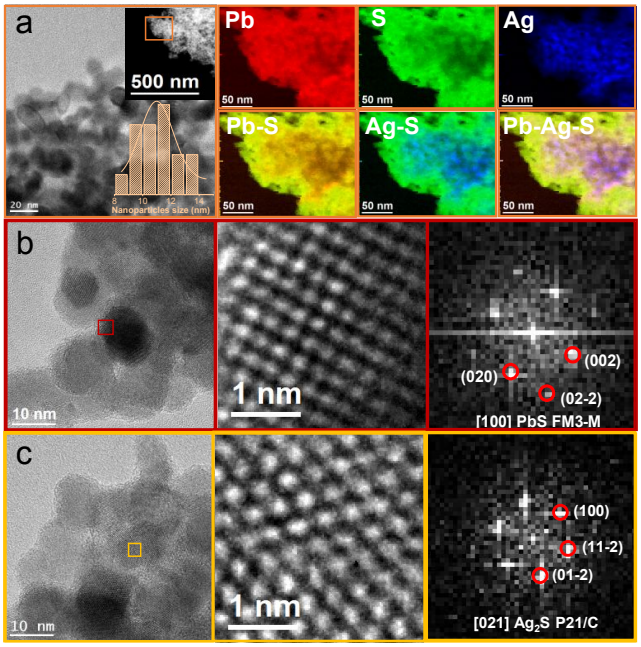

Figure 2. a) Representative TEM micrographs of $Pb_{0.95}Ag_{0.05}S$ nanoparticles and histogram of the particle size distribution (inset), EELS chemical composition maps. b,c) HRTEM micrographs of a $Pb_{0.95}Ag_{0.05}S$ sample, and their corresponding electron diffraction patterns.

Figure 3 shows the measured σ, S and Hall effect of the $Pb_{1-x}Ag_xS$ pellets. The σ of the pure PbS sample is inherently low, rendering it impractical for measuring at room temperature. This conductivity escalates with temperature as it corresponds to an intrinsic or moderately doped semiconductor (**Figure 3a**). With Ag doping, the σ experiences a notable surge, but maintains its dependence with temperature below 650 K, where σ peaks before gradually declining. The rise in σ with Ag doping primarily stems from the increase of hole concentration (p). In addition, the decline in conductivity beyond 650 K predominantly arises from the gradual decrease of mobility experience by the high density of thermally excited bipolar carriers at this temperature.

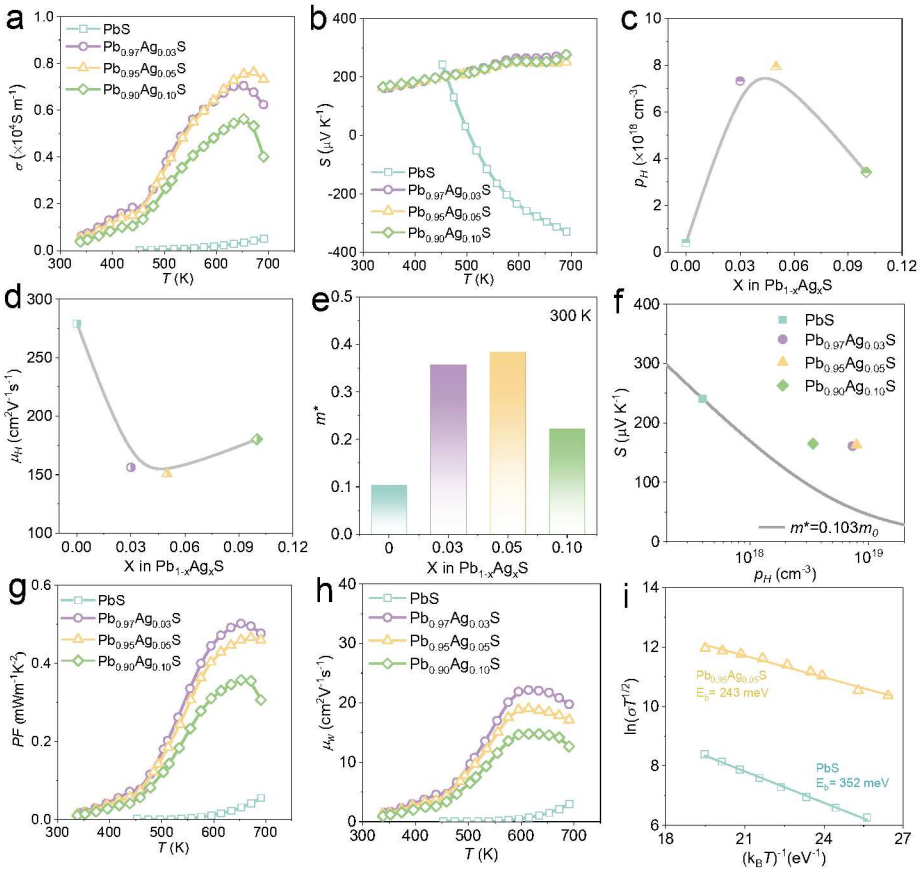

Figure 3. a-h) Thermoelectric properties of $Pb_{1-x}Ag_xS$ pellets. a) Temperature dependence of electric conductivity. b) Temperature dependence of Seebeck coefficient (S). c) Ambient temperature Hall carrier concentration (p_H), d) carrier mobility (μ_H) and e) effective mass (m^*). f) Pisarenko plot. g) Power factors (PF). h) Temperature dependence of weighted mobility (μ_W). i) Energy barrier scattering in PbS and $Pb_{0.95}Ag_{0.05}S$ pellets.

PbS exhibits a positive Seebeck coefficient at temperatures below 500 K and becomes negative S at higher temperature (**Figure 3b**). The p-type semiconductor characteristic at low temperatures is primarily attributed to the presence of PbO on the surface of the nanoparticles grown during the synthesis process or the posterior exposition of the particles to air, and which inherently exhibits p-type semiconductor properties. As temperature rises, the concentration of thermally generated charge carriers gradually surpasses the density of holes associated with the presence of PbO and the intrinsic n-type characteristics of PbS become predominant. In contrast, all the

Ag-doped samples consistently display a p-type semiconductor characteristic across the entire temperature range. This variation primarily stems from the substitution of Pb^{2+} with Ag^{+}, which leads to an increase in hole concentration.

Hall measurements at room temperature were conducted to determine the Hall hole concentration (p_H)and mobility (μ_H) as shown in **Figure 3c** and **3d**. The p_H of PbS is 4.0×10^{17} cm^{-3} and increases significantly when doped with a low content of Ag. The p_H of $Pb_{0.95}Ag_{0.05}S$ is 7.9×10^{18} cm^{-3}, about one order of magnitude higher than PbS, which is associated with the acceptor role played by Ag^{+} ions at the Pb^{+} sites within the PbS lattice. The p_H decreased in samples with high Ag content, possibly due to an increase in the nucleated Ag_2S domains. As anticipated, μ_H decreases with Ag doping, which is related to the increase of atomic scattering centers and the distorted lattice.

Effective mass (m*) values were estimated using a single parabolic band (SPB) model, thereby encompassing the overall contribution from multiple valence bands in the estimation. **Figure 3e** illustrates that Ag doping leads to an increase in the m* since the downward of Fermi level to valence band. **Figure 3f** displays the Pisarenko plot including the S and p_H of all the samples at room temperature. The S of the samples containing Ag are slightly above the theoretical curve plotted considering the m* of PbS. This result is consistent with the electronic band structure calculations below.

The σ and S values of $Pb_{1-x}Ag_xS$ were used to compute the power factors ($PF = \sigma S^2$) as depicted in **Figure 3g**. The PFs of the Ag-doped samples were significantly higher than those of PbS, and they demonstrated a significant enhancement with rising temperature up to 650 K. Above 650 K, the PFs of the Ag-doped samples experienced a slight decrease, associated with the decreased electrical conductivity. The highest PF value reached 0.51 $mWm^{-1}K^{-2}$ at 650 K, obtained from the $Pb_{0.97}Ag_{0.03}S$ sample. This value is much higher than that of PbS, which displayed a maximum PF value of 0.03 $mWm^{-1}K^{-2}$ at 650 K.

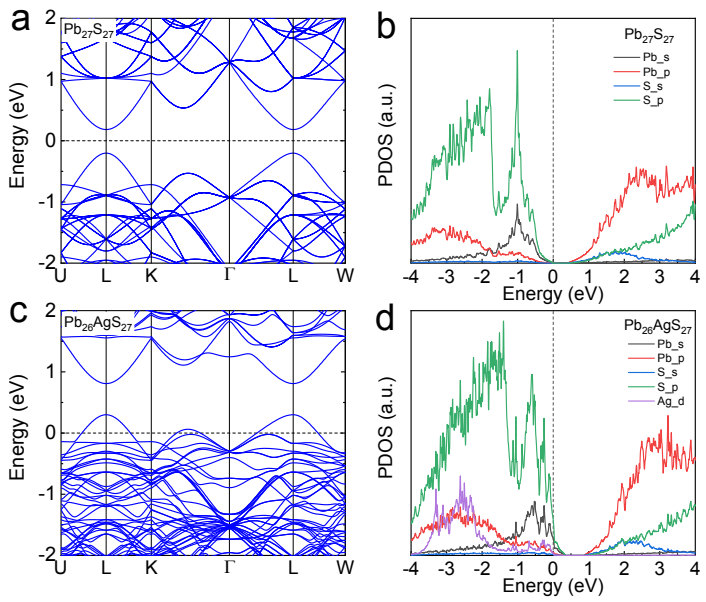

Figure 4. (a, c) Calculated electronic band structure and (b, d) density of states for PbS and Ag-doped PbS, respectively. The deashed line refers to Fermi level.

To explore the influence of Ag doping on the electronic band structure of PbS, we conducted density functional theory (DFT) calculations. **Figure 4** shows the calculated electronic band structure and density of states (DOS) of PbS and Ag-doped PbS. The electronic band structure illustrates that upon the substitution of Pb with Ag, the Fermi level shifts into the valence band, thereby attaining p-type semiconductor characteristics. Additionally, the introduction of Ag doping resulted in an augmentation of the band gap of PbS from 0.38 eV to 0.48 eV. Furthermore, there's a reduction in the energy difference between L and Σ valleys, indicating a tendency towards energy band convergence, which is poised to enhance the power factor. Following Ag doping, a substantial increase is observed in the DOS slope at the Fermi level, thereby aiding in the enhancement of the m^* and Seebeck coefficient.

The weighted mobility (μ_W) was calculated using σ and S values, providing a mobility parameter unaffected by p_H. This calculation considers the average mobility across all conductive channels, thus offering a comprehensive assessment of the overall conductivity[33]. Detailed calculation formulas can be found in the SI. μ_W increases with Ag doping (**Figure 3h**). The $Pb_{0.97}Ag_{0.03}S$ sample exhibited the highest μ_W value at 22.1

$cm^2V^{-1}s^{-1}$ at 613 K, which denotes superior electrical transport properties. The observed variations in mobility often suggest a hopping process or energy barrier scattering. Here, we consider a grain boundary barrier scattering mechanism to describe mobility, a model that has been extensively applied to thermoelectric materials. Assuming a uniformly distributed concentration of ionized carrier traps and barrier, and a grain boundary thickness that is much less than the crystallite size L, the effective mobility (μ) is given by[34]

$$\mu = Le\left(\frac{1}{2\pi m^* k_B T}\right)^{1/2} \exp\left(\frac{-E_B}{k_B T}\right) \quad (1)$$

where E_B is the energy barrier. A clearly linear relationship is seen between $\ln(\mu T^{1/2})$ and $(k_B T)^{-1}$ in **Figure 3i**, with a slope equal to E_B. E_B was decreased from 352 meV to 243 meV with Ag doping. This indicates that Ag doping reduces the grain boundary barrier and increases the effective mobility, which is consistent with the results in **Figure 3h**.

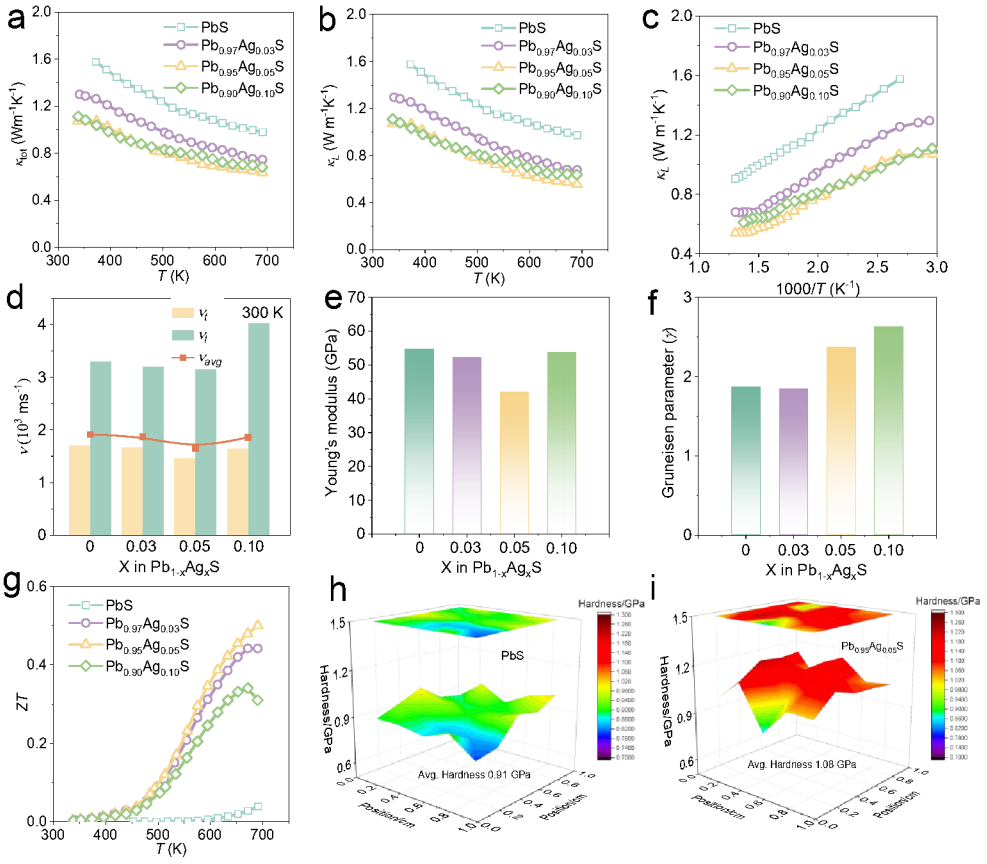

Figure 5. a-c) Thermoelectric properties of $Pb_{1-x}Ag_xS$ pellets. Temperature dependence of a)

thermal conductivity (κ_{total}) and b) lattice thermal conductivity (κ_L). c) The plot of 1000/T-dependent κ_L. d) Sound velocity, e) Young's modulus (E) and f) Grüneisen parameter (γ) of $Pb_{1-x}Ag_xS$ pellets at room temperature. g) ZT value. h-i) 3D cloud diagram of hardness for PbS and $Pb_{0.95}Ag_{0.05}S$ pellets. i) Average modulus and average hardness of PbS and $Pb_{0.95}Ag_{0.05}S$ pellets.

The κ_{total} values of all the $Pb_{1-x}Ag_xS$ (x = 0, 0.03, 0.05, 0,10) samples are shown in **Figure 5a**. Ag doping significantly reduced the κ_{total}. We calculate κ_{ele} (**Figure S4**) and κ_L (**Figure 5b**) of all the samples by the Wiedemann-Franz law, $\kappa_{ele}=L_o\sigma T$ and $\kappa_L=\kappa_{total}-\kappa_{ele}$, where L_o is the Lorenz number $\sim 1.7\times10^{-8}$ V^2K^{-2} obtained from the measured S values (**Figure S5**). **Figure 5b** shows that Ag doping significantly reduces the κ_L of the sample over the entire temperature range, especially for $Pb_{0.95}Ag_{0.05}S$ that reaches 0.48 W $m^{-1}K^{-1}$ at 690 K. This reduction in κ_L, is related to a multiscale phonon scattering phenomena that includes the introduced point defects, the lattice dislocation caused by Ag doping, and the multi-grain boundary introduced by the secondary phase. **Figure 5c** shows the plot of 1000/T-dependent κ_L for all samples. Only the undoped sample shows a roughly linear relationship, indicating that the Umklapp phonon scattering plays a critical role in PbS[22]. Ag-doped samples display a notably restrained bipolar thermal conductivity in contrast to that of the pristine PbS at high temperature, which might be ascribed to the diminished bipolar diffusion owing to the increased band gap[11].

In pursuit of a deeper comprehension of the mechanism underlying the achieved ultra-low κ_L, we conducted measurements of the sound velocity of the samples at room temperature. The κ_L is related to the average sound velocity (v_{avg}), Grüneisen parameter (γ), Young's modulus (E), etc. This relationship is commonly described by the Debye-Callaway equation[15]:

$$\kappa_L = \frac{1}{3}C_v v_{\mathrm{avg}} l \quad (2)$$

where C_v is the specific heat derived from the Dulong–Petit limit and l is the phonon mean free path. The v_{avg} is calculated from the longitudinal (v_l) and shear velocity (v_t)[6,20]:

$$v_{\text{avg}} = [\frac{1}{3}(\frac{1}{v_l^3} + \frac{2}{v_t^3})]^{-1/3} \quad (3)$$

The v_l and v_t can be acquired directly in the ultrasonic pulse echo measurements, shown in **Figure 5d**. The v_{avg} decreases with Ag doping, and achieved a minimum value of 1.6×10^3 m s^{-1} in $Pb_{0.95}Ag_{0.05}S$. The decrease of sound velocity may be due to the weaker interatomic bonding between Ag and S.

According to the Debye model, there is a relationship between l and the phonon lifetime τ: $l = v_{avg}\tau$. The τ can be calculated using the Grüneisen parameter (γ) and the Young's modulus (E), typically approximated as[35]:

$$\tau = \frac{\hbar}{2k_B T\gamma E} \frac{1}{} \quad (4)$$

The E and γ can be calculated from the sound velocity, shown in **Figure 5e-f and Table S2**. Detailed calculation formulas can be found in the SI. The E decreases slightly with Ag doping, but γ increases significantly, from 1.87 in PbS to 2.37 in $Pb_{0.95}Ag_{0.05}S$. Hence, the notably low κ_L of $Pb_{0.95}Ag_{0.05}S$, attributed to its lower phonon transmission velocity and larger γ. In addition, shear modulus and Poisson ratio also can be calculated from the sound velocity[20], which also related to the κ_L (**Table S2**).

Overall, the combination of enhanced electrical and degraded thermal transport properties resulted in a peak ZT value of 0.5 at 690 K for $Pb_{0.95}Ag_{0.05}S$, significantly surpassing that of undoped PbS (**Figures 5g**). Moreover, the mechanical properties of the bulk samples were evaluated using nanoindentation, using the Nano-Blitz 3D method. Analysis of 3D hardness diagrams indicates a notable increase in hardness for the $Pb_{0.95}Ag_{0.05}S$ sample compared to the PbS sample, the average hardness increased from 0.91 GPa in PbS to 1.08 GPa in $Pb_{0.95}Ag_{0.05}S$ (**Figure 5h-i**). The improvement in mechanical hardness is typically associated with alterations in the crystal structure and chemical composition of the material[36]. In the hot-press process, partial Ag replacement of Pb introduces point defects, lattice dislocation and the Ag_2S secondary phase. The introduction of this second phase can elevate the density of dislocations and barriers within the material, thereby hindering the movement and slipping of dislocations[6,13]. This increased structural complexity enhances the material's resistance to deformation and plasticity, ultimately improving its mechanical strength.

In summary, we reported a straightforward aqueous synthesis method to produce Ag-doped PbS nanocrystals with high yield and scalability. The bulk composites were prepared by hot pressing, and the effect of Ag doping on the thermoelectric properties and mechanical hardness of PbS was discussed. DFT calculations revealed that the presence of Ag promoted band convergence and shifted the Fermi level towards the valence band, which resulted in p-type semiconductor characteristics. Furthermore, through structural analysis, we showed that a portion of Ag exists as a secondary phase of Ag_2S, which increases the interfacial density within the sample, consequently enhancing phonon scattering and reducing lattice thermal conductivity. This alteration in microstructure by Ag doping also resulted in an enhancement of the mechanical hardness of the material. Overall, this study demonstrated an enhancement of the thermoelectric properties and mechanical hardness of PbS by optimizing both band structure and microstructure, which provides a solid experimental basis for the potential commercialization of systems based of this or related thermoelectric materials.

AUTHOR INFORMATION

Corresponding Author

* Email: wangdongyang@zzu.edu.cn

* Email: mcjia@zzu.edu.cn

* Email: acabot@irec.cat

Author Contributions

The manuscript was written through contributions of all authors. All authors have given approval to the final version of the manuscript.

Notes

The authors declare no competing financial interest.

ACKNOWLEDGEMENT

This work was supported by China Postdoctoral Science Foundation under Grant Number 2023M743151. D.W. acknowledges funding from the National Natural Science Foundation of China (Nos. 12204156), and the China Postdoctoral Science Foundation (Nos. 2023QT0315 and 2023M743223). M.J. acknowledges funding from the China Postdoctoral Science Foundation (No. 2023M743221). ICN2 acknowledges funding from Generalitat de Catalunya 2021SGR00457. A.C. thanks the support from the projects ENE2016-77798-C4-3-R and NANOGEN (PID2020-116093RB-C43), funded by MCIN/ AEI/10.13039/501100011033/ and by "ERDF A way of making Europe", by the "European Union".

REFERENCES

(1) Xing, C.; Zhang, Y.; Xiao, K.; Han, X.; Liu, Y.; Nan, B.; Ramon, M. G.; Lim, K. H.; Li, J.; Arbiol, J.; Poudel, B.; Nozariasbmarz, A.; Li, W.; Ibáñez, M.; Cabot, A. Thermoelectric Performance of Surface-Engineered $Cu_{1.5-x}Te$-Cu_2Se Nanocomposites. *ACS Nano* **2023**, *17* (9), 8442–8452.

(2) Liu, Y.; Zhang, Y.; Ortega, S.; Ibáñez, M.; Lim, K. H.; Grau-Carbonell, A.; Martí-Sánchez, S.; Ng, K. M.; Arbiol, J.; Kovalenko, M. V.; Cadavid, D.; Cabot, A. Crystallographically Textured Nanomaterials Produced from the Liquid Phase Sintering of $Bi_xSb_{2-x}Te_3$ Nanocrystal Building Blocks. *Nano Lett.* **2018**, *18* (4), 2557–2563.

(3) Gan, L.; Zhang, F.; Zhao, X.; Zhong, Y.; Deng, Q.; Zhang, K.; Ang, R. Thermoelectric Enhancement for n-Type PbS via Synergistic Effect of Ti Doping and Cu_2S Compositing. *Appl. Phys. Lett.* **2023**, *122* (3), 032101.

(4) Su, W.; Deng, Q.; Gan, L.; Tan, X.; He, Z.; Yuan, W.; Zhao, C.; An, X.; Liu, B.; Ang, R. Ultra-High Thermoelectric Performance Achieved in Only Ternary

Lead Sulfide through Unconventional Halogen Element Doping. *Mater. Today Phys.* **2024**, *42*, 101364.

(5) Ma, B.; Li, Y.; Zhu, L.; Zhang, F.; Li, X.; Shi, Y.; Liang, P.; Peng, Z.; Chao, X.; Yang, Z.; Wu, D. Modulation Doping Promoted Ultrahigh Electron Mobility and Enhanced Thermoelectric Performance in PbTe. *Chem. Eng. J.* **2024**, *488*, 150647.

(6) Zhang, Y. X.; Huang, Q. Y.; Yan, X.; Wang, C. Y.; Yang, T. Y.; Wang, Z. Y.; Shi, Y. C.; Shan, Q.; Feng, J.; Ge, Z. H. Synergistically Optimized Electron and Phonon Transport in High-Performance Copper Sulfides Thermoelectric Materials via One-Pot Modulation. *Nat. Commun.* **2024**, *15*, 2736.

(7) Gan, L.; Zhang, F.; Wang, M.; Deng, Q.; Su, W.; Zhang, K.; Ang, R. The Thermoelectric Performance in Transition Metal-Doped PbS Influenced by Formation Enthalpy. *Appl. Phys. Lett.* **2023**, *123* (19), 192103.

(8) Liu, Y.; Calcabrini, M.; Yu, Y.; Lee, S.; Chang, C.; David, J.; Ghosh, T.; Spadaro, M. C.; Xie, C.; Cojocaru-Mirédin, O.; Arbiol, J.; Ibáñez, M. Defect Engineering in Solution-Processed Polycrystalline SnSe Leads to High Thermoelectric Performance. *ACS Nano* **2022**, *16* (1), 78–88.

(9) Liu, Y.; Calcabrini, M.; Yu, Y.; Lee, S.; Chang, C.; David, J.; Ghosh, T.; Spadaro, M. C.; Xie, C.; Cojocaru-Mirédin, O.; Arbiol, J.; Ibáñez, M. Defect Engineering in Solution-Processed Polycrystalline SnSe Leads to High Thermoelectric Performance. *ACS Nano* **2021**.

(10) Li, M.; Liu, Y.; Zhang, Y.; Zuo, Y.; Li, J.; Lim, K. H.; Cadavid, D.; Ng, K. M.; Cabot, A. Crystallographically Textured SnSe Nanomaterials Produced from the Liquid Phase Sintering of Nanocrystals. *Dalt. Trans.* **2019**, *48* (11), 3641–3647.

(11) Chang, C.; Liu, Y.; Ho Lee, S.; Chiara Spadaro, M.; Koskela, K. M.; Kleinhanns, T.; Costanzo, T.; Arbiol, J.; Brutchey, R. L.; Ibáñez, M. Surface Functionalization of Surfactant-Free Particles: A Strategy to Tailor the Properties of Nanocomposites for Enhanced Thermoelectric Performance. *Angew. Chemie* **2022**, *134* (35), e202207002.

(12) Li, M.; Liu, Y.; Zhang, Y.; Han, X.; Zhang, T.; Zuo, Y.; Xie, C.; Xiao, K.; Arbiol, J.; Llorca, J.; Ibáñez, M.; Liu, J.; Cabot, A. Effect of the Annealing Atmosphere on Crystal Phase and Thermoelectric Properties of Copper Sulfide. *ACS Nano* **2021**, *15* (3), 4967–4978.

(13) Lou, L. Y.; Yang, J.; Zhu, Y. K.; Liang, H.; Zhang, Y. X.; Feng, J.; He, J.; Ge, Z. H.; Zhao, L. D. Tunable Electrical Conductivity and Simultaneously Enhanced Thermoelectric and Mechanical Properties in N-Type Bi_2Te_3. *Adv. Sci.* **2022**, *9* (27), 23–25.

(14) Chen, Z.; Cui, H. H.; Hao, S.; Liu, Y.; Liu, H.; Zhou, J.; Yu, Y.; Yan, Q.; Wolverton, C.; Dravid, V. P.; Luo, Z. Z.; Zou, Z.; Kanatzidis, M. G. GaSb Doping Facilitates Conduction Band Convergence and Improves Thermoelectric Performance in N-Type PbS. *Energy Environ. Sci.* **2023**, *16* (4), 1676–1684.

(15) Zhang, R.; Pei, J.; Han, Z.; Wu, Y.; Zhao, Z.; Zhang, B. Fabricated Via High-Pressure Process At Room Temperature. *J. Adv. Ceram.* **2020**, *9* (4), 535–543.

(16) Xie, S.; Liu, K.; Li, C.; Yan, F.; Ouyang, Y.; Ge, H.; Li, X.; Su, X.; Liu, Y.; Liu, W.; Tang, X. Revealing the Temperature-Driven Lifshitz Transition in p-Type Mg_3Sb_2-Based Thermoelectric Materials. *Appl. Phys. Lett.* **2024**, *124* (9), 093902.

(17) Cao, Y.; Dai, S.; Wang, X.; Wei, T.; Yang, J.; Xi, L.; Pang, Z.; Tan, G. High-Throughput Screening of Potentially Ductile and Low Thermal Conductivity ABX_3 (X = S, Se, Te) Thermoelectric Perovskites. *Appl. Phys. Lett.* **2024**, *124* (9), 092101.

(18) Bai, C.; Wang, J.; Ding, M.; Lang, Y.; Pan, L.; Wang, Y.; He, S.; Wan, C.; Ahmad, K.; Almutairi, Z. Prominent Texturing and Enhanced Thermoelectric Performance of Misfit Layered $(PbS)_{1.18}(TiS_2)_2$ via an Exfoliation-Restacking Approach. *J. Alloys Compd.* **2024**, *976*, 173032.

(19) Shao, K.; Zhou, D.; Yang, M.; Zhu, H.; Fan, H.; Su, T. Facile Synthesize and Enhanced Thermoelectric Performance of PbS with Cl Doping and PbSe Alloying. *J. Alloys Compd.* **2024**, *977*, 173413.

(20) Xiao, Y.; Chang, C.; Pei, Y.; Wu, D.; Peng, K.; Zhou, X.; Gong, S.; He, J.; Zhang, Y.; Zeng, Z.; Zhao, L. D. Origin of Low Thermal Conductivity in SnSe. *Phys. Rev. B* **2016**, *94* (12), 5–10.

(21) Liu, W.; Xu, L.; Xiao, Y.; Zhao, L. D. Strategies to Advance Earth-Abundant PbS Thermoelectric. *Chem. Eng. J.* **2023**, *465*, 142785.

(22) Jiang, B.; Liu, X.; Wang, Q.; Cui, J.; Jia, B.; Zhu, Y.; Feng, J.; Qiu, Y.; Gu, M.; Ge, Z.; He, J. Realizing High-Efficiency Power Generation in Low-Cost PbS-Based Thermoelectric Materials. *Energy Environ. Sci.* **2020**, *13* (2), 579–591.

(23) Li, M.; Liu, Y.; Zhang, Y.; Han, X.; Xiao, K.; Nabahat, M.; Arbiol, J.; Llorca, J.; Iban, M.; Cabot, A. PbS−Pb−Cu_xS Composites for Thermoelectric Application. *ACS Appl. Mater. Interfaces* **2021**.

(24) Li, M.; Liu, Y.; Zhang, Y.; Chang, C.; Zhang, T.; Yang, D.; Xiao, K.; Arbiol, J.; Ibáñez, M.; Cabot, A. Room Temperature Aqueous-Based Synthesis of Copper-Doped Lead Sulfide Nanoparticles for Thermoelectric Application. *Chem. Eng. J.* **2022**, *433* (November 2021), 133837.

(25) Calcabrini, M.; Genç, A.; Liu, Y.; Kleinhanns, T.; Lee, S.; Dirin, D. N.; Akkerman, Q. A.; Kovalenko, M. V.; Arbiol, J.; Ibáñez, M. Exploiting the Lability of Metal Halide Perovskites for Doping Semiconductor Nanocomposites. *ACS Energy Lett.* **2021**, *6* (2), 581–587.

(26) Ibáñez, M.; Genç, A.; Hasler, R.; Liu, Y.; Dobrozhan, O.; Nazarenko, O.; De La Mata, M.; Arbiol, J.; Cabot, A.; Kovalenko, M. V. Tuning Transport Properties in Thermoelectric Nanocomposites through Inorganic Ligands and Heterostructured Building Blocks. *ACS Nano* **2019**, *13* (6), 6572–6580.

(27) Qin, Y.; Hong, T.; Qin, B.; Wang, D.; He, W.; Gao, X.; Xiao, Y.; Zhao, L. D. Contrasting Cu Roles Lead to High Ranged Thermoelectric Performance of PbS. *Adv. Funct. Mater.* **2021**, *31*, 2102185.

(28) Li, M.; Liu, Y.; Zhang, Y.; Han, X.; Xiao, K.; Nabahat, M.; Arbiol, J.; Llorca, J.; Iban, M.; Cabot, A. PbS−Pb−Cu_xS Composites for Thermoelectric Application. *ACS Appl. Mater. Interfaces* **2021**, *13*, 51373–51382.

(29) Laing, M. The Electronegativity of a Metal and Its E°: Should They Correlate? *S. Afr. J. Sci.* **2002**, *98* (11–12), 573–580.

(30) Sun, R.; Jia, M.; Chen, X.; Zhang, F.; Ma, Z.; Liu, Y.; Zhang, J.; Lian, L.; Han, Y.; Li, M.; Yang, D.; Li, X.; Zhang, Y.; Shan, C.; Shi, Z. Constructing Efficient and Thermostable Red-NIR Emitter via Cross Relaxation and Crystal-Field Engineering of Holmium-Based Perovskite-Type Half Metal. *Laser Photonics Rev.* **2023**, 2301028.

(31) Liu, Z.; Ji, X.; Ma, Z.; Zhang, F.; Qi, X.; Chen, X.; Wu, D.; Liu, Y.; Jia, M.; Li, X.; Zhang, Y.; Shan, C.; Shi, Z. Healthy and High-Quality Single-Source Lighting Based on Double-Doped Tin Halide Engineering. *Laser Photonics Rev.* **2023**, *17* (9), 2300094.

(32) Zang, P.; Du, Y.; Yu, C.; Yang, D.; Gai, S.; Feng, L.; Liu, S.; Yang, P.; Lin, J. Photothermal-Actuated Thermoelectric Therapy by Harnessing Janus-Structured Ag-Ag_2S Nanoparticles with Enhanced Antitumor Efficacy. *Chem. Mater.* **2023**, *35* (18), 7770–7780.

(33) Qin, B.; He, W.; Zhao, L. D. Estimation of the Potential Performance in P-Type SnSe Crystals through Evaluating Weighted Mobility and Effective Mass. *J. Mater.* **2020**, *6* (4), 671–676.

(34) Wei, T. R.; Wu, C. F.; Zhang, X.; Tan, Q.; Sun, L.; Pan, Y.; Li, J. F. Thermoelectric Transport Properties of Pristine and Na-Doped $SnSe_{1-x}Te_x$ Polycrystals. *Phys. Chem. Chem. Phys.* **2015**, *17* (44), 30102–30109.

(35) Mohanta, M. K.; Rawat, A.; Jena, N.; Ahammed, R.; De Sarkar, A. Superhigh Flexibility and Out-of-Plane Piezoelectricity Together with Strong Anharmonic Phonon Scattering Induced Extremely Low Lattice Thermal Conductivity in Hexagonal Buckled CdX (X = S, Se) Monolayers. *J. Phys. Condens. Matter* **2020**, *32*, 355301.

(36) Liang, H.; Lou, Q.; Zhu, Y. K.; Guo, J.; Wang, Z. Y.; Gu, S. W.; Yu, W.; Feng, J.; He, J.; Ge, Z. H. Highly Enhanced Thermoelectric and Mechanical Properties of Bi-Sb-Te Compounds by Carrier Modulation and Microstructure Adjustment.

ACS Appl. Mater. Interfaces **2021**, *13* (38), 45589–45599.

Table of Contents